Electronic State Structure and Optical Properties of $Tb(oda)_3^{3-}$ Complexes in Trigonal $Na_3[Tb(oda)_3]\cdot 2NaClO_4\cdot 6H_2O$ Crystals†

Todd A. Hopkins, David H. Metcalf, and F. S. Richardson*

Department of Chemistry, University of Virginia, Charlottesville, Virginia 22901

Received August 29, 1997

Polarized optical absorption and emission measurements are used to locate and assign 95 crystal-field energy levels split out of the $4f^8$ electronic configuration of Tb^{3+} in single crystals of $Na_3[Tb(oda)_3]\cdot 2NaClO_4\cdot 6H_2O$ (where oda denotes an oxydiacetate ligand). The absorption measurements span the 235−490 nm wavelength range, and the emission measurements span the 485−685 nm wavelength range. The combined absorption and emission spectra measurements provide access to the energy-level structures of 46 different $4f^8[SL]J$ multiplet manifolds of Tb^{3+} (*all* multiplet manifolds with baricenter energies $<42\,400$ cm^{-1} above ground). The site symmetry of the Tb^{3+} ions in $Na_3[Tb(oda)_3]\cdot 2NaClO_4\cdot 6H_2O$ is D_3, and the point-group symmetry of the tris-terdentate $Tb(oda)_3^{3-}$ coordination complexes is also D_3. The $Tb(oda)_3^{3-}$ complexes are chiral, and they exist in just one, fully resolved enantiomeric form in single crystals of $Na_3[Tb(oda)_3]\cdot 2NaClO_4\cdot 6H_2O$. The crystals exhibit strong chiroptical activity in their absorption *and* emission spectra, and results obtained from both circularly polarized and linearly polarized optical spectra measurements are used in making transition line assignments. The energy-level data acquired from the spectroscopic measurements are analyzed in terms of a model Hamiltonian that includes consideration of both isotropic and nonisotropic 4f electron/crystal-field interactions, and the interaction parameters derived from this analysis are discussed and then compared with those obtained for other $Na_3[Ln(oda)_3]\cdot 2NaClO_4\cdot 6H_2O$ systems *and* for Tb^{3+} in other crystalline hosts.

Introduction

The tris-terdentate coordination complexes formed by the chelation of three oxydiacetate (oda) ligands to a trivalent lanthanide ion (Ln^{3+}) have been studied extensively to elicit information about the effects of ligand structural complexity on the details of $Ln^{3+}(4f^N)$ electronic state structure and optical properties. In these complexes, denoted here by $Ln(oda)_3^{3-}$, each oda ligand is coordinated to the lanthanide ion via two negatively charged oxygen atoms (one from each of the two carboxylate moieties in oda) and a neutral ether oxygen atom. The LnO_9 coordination cluster in these complexes forms a slightly distorted tri-capped trigonal-prism polyhedron of trigonal-dihedral (D_3) symmetry, with the top and bottom triangles of this polyhedron defined by carboxylate oxygen donor atoms and the capping positions (on normals to the rectangular faces) occupied by ether oxygen atoms. The backbone of each bicyclic Ln(oda) chelate ring system is nearly planar and stretches diagonally across a rectangular face of the LnO_9 trigonal-prism structure. The chelate rings contain highly anisotropic charge distributions, and their interactions with the lanthanide 4f electrons produce effects not ordinarily observed in structurally simpler systems.

The equilibrium structures of $Ln(oda)_3^{3-}$ complexes have trigonal-dihedral (D_3) symmetry, and in aqueous solution these complexes exist as a racemic mixture of rapidly interconverting optical isomers (enantiomers) which are often denoted as Λ-$Ln(oda)_3^{3-}$ and Δ-$Ln(oda)_3^{3-}$. However, in single crystals of $Na_3[Ln(oda)_3]\cdot 2NaClO_4\cdot 6H_2O$ grown from aqueous solution, all of the $Ln(oda)_3^{3-}$ complexes are of like enantiomeric form (either Λ or Δ), and these crystals exhibit chiroptical properties that have proved to be useful in characterizing the electronic energy-level structures and optical transition mechanisms in $Ln(oda)_3^{3-}$ complexes.[1,2] At room temperature, these crystals have trigonal, *R*32 space-group symmetry, with three $Ln(oda)_3^{3-}$ complexes per unit cell and with the Ln^{3+} ions located at sites of D_3 point-group symmetry.[3−6] The macroscopic uniaxial symmetry of these crystals is generally maintained over extended temperature ranges below 300 K, though for several members of the lanthanide series there is spectroscopic evidence that the Ln^{3+} site symmetry is lower than D_3 at temperatures below 120 K.[2] Optical-quality single crystals of $Na_3[Ln(oda)_3]\cdot 2NaClO_4\cdot 6H_2O$ compounds are relatively easy to grow, and they have been used extensively in detailed studies of electronic state structure and optical processes in $Ln(oda)_3^{3-}$ complexes. Among these complexes, the most thoroughly studied have been those of neodymium (Nd^{3+}),[7−11] samarium (Sm^{3+}),[12−15] europium (Eu^{3+}),[16−19] gadolinium (Gd^{3+}),[20−23] dysprosium (Dy^{3+}),[24]

* To whom correspondence should be addressed.
† "oda" is oxydiacetate ($^-OOCCH_2OCH_2COO^-$).

(1) Richardson, F. S.; Faulkner, T. R. *J. Chem. Phys.* **1982**, *76*, 1595.
(2) Richardson, F. S. *J. Less-Common Met.* **1989**, *149*, 161.
(3) Albertsson, J. *Acta Chem. Scand.* **1968**, *22*, 1563.
(4) Albertsson, J. *Acta Chem. Scand.* **1970**, *24*, 3527.
(5) Albertsson, J.; Elding, I. *Acta Chem. Scand., Ser. A* **1977**, *31*, 21.
(6) Fronczek, F. R.; Banerjee, A. K.; Watkins, S. F.; Schwartz, R. W. *Inorg. Chem.* **1981**, *20*, 2745.
(7) Vala, M.; Szczepanski, J.; Banerjee, A. K.; Chowdhury, M. *Chem. Phys.* **1989**, *134*, 149.
(8) May, P. S.; Jayasankar, C. K.; Richardson, F. S. *Chem. Phys.* **1989**, *138*, 123.
(9) May, P. S.; Jayasankar, C. K.; Richardson, F. S. *Chem. Phys.* **1989**, *138*, 139.
(10) May, P. S. Ph.D. Dissertation, University of Virginia, 1988.
(11) Fluyt, L.; Couwenberg, I.; Lambaerts, H.; Binnemans, K.; Görller-Walrand, C.; Reid, M. F. J. Chem. Phys. **1996**, *105*, 6117.
(12) May, P. S.; Reid, M. F.; Richardson, F. S. *Mol. Phys.* **1987**, *61*, 1455.
(13) May, P. S.; Reid, M. F.; Richardson, F. S. *Mol. Phys.* **1987**, *61*, 1471.
(14) May, P. S.; Reid, M. F.; Richardson, F. S. *Mol. Phys.* **1987**, *62*, 341.

S0020-1669(97)01114-2 CCC: $15.00
Published on Web 02/26/1998

holmium (Ho^{3+}),[25−27] and erbium (Er^{3+}).[28,29] Optical studies of the praseodymium (Pr^{3+}),[30] terbium (Tb^{3+}),[31] and thulium (Tm^{3+})[32] complexes have also been reported, but without detailed analyses of energy-level structure.

In the present paper, we report the first detailed analysis of $4f^8(Tb^{3+})$ electronic energy-level structure in $Tb(oda)_3^{3-}$ complexes, using data obtained from optical (and chiroptical) absorption and emission measurements performed on single crystals of $Na_3[Ln(oda)_3]\cdot 2NaClO_4\cdot 6H_2O$, which we shall denote hereafter as TbODA. The $4f^8$ electronic energy-level structure of Tb^{3+} in TbODA presented a somewhat more difficult challenge for measurement and analysis than was encountered in our previous work on other $Ln(oda)_3^{3-}$ (and LnODA) systems, but eventually the combined measurement and analysis techniques permitted the location and symmetry assignment of 95 (of the 314 total) crystal-field levels split out of the 46 lowest-energy $4f^8[SL]J$ multiplet manifolds of Tb^{3+} in TbODA. These levels span the 0−42 400 cm^{-1} energy range (above ground), and they provided an adequate basis for performing parametric modeling calculations of crystal-field interaction strengths in TbODA. The parametrized model Hamiltonian derived from these calculations produced an eigenvalue spectrum in which the rms deviation between calculated and observed energy levels is <12 cm^{-1}. The overall crystal-field interaction strength determined for $Tb^{3+}(4f^8)$ in TbODA is found to be somewhat greater than that determined for $Tb^{3+}(4f^8)$ in single crystals of $Na_3[Yb_{0.95}Tb_{0.05}(dpa)_3]\cdot NaClO_4\cdot 10H_2O$, where in the latter the Tb^{3+} ions are each coordinated to three dipicolinate (dpa) ligands via tris-terdentate chelation.[33] The overall crystal-field interaction strength determined for TbODA is also greater than those determined for any of the other LnODA systems that have been studied so far.

The experimental work performed in the study reported here included measurements of unpolarized, circularly polarized, and σ and π linearly polarized optical absorption and emission spectra, under variable sample-temperature conditions. The absorption spectra measurements spanned the 235−490 nm wavelength range, and the emission spectra measurements spanned the 485−685 nm wavelength range. All of the luminescence observed for TbODA originates from the lowest $^5D_4$ multiplet manifold of $Tb^{3+}(4f^8)$, which is centered at ca. 20 480 cm^{-1} above ground. The emission spectra recorded for TbODA encompass all transitions that originate from this $^5D_4$ multiplet manifold and terminate on levels split out of the seven ^7F_J ($J = 0-6$) multiplet manifolds derived from the ^7F (*ground*) term of the $4f^8(Tb^{3+})$ electronic configuration. The lowest-energy (*ground*) multiplet of $4f^8(Tb^{3+})$ is $^7F_6$, and all transitions observed in the recorded absorption spectra originate from crystal-field (Stark) levels split out of this multiplet manifold. In a crystal field of trigonal-dihedral (D_3) symmetry, the $^7F_6$ multiplet is split into nine Stark levels, four of which are doubly degenerate. In TbODA, the total splitting between the lowest- and highest-energy Stark levels of $^7F_6$ is only about 200 cm^{-1}, so under room-temperature conditions all nine of the Stark levels split out of $^7F_6$ are thermally accessible.

Experimental Methods

Compound and Crystal Sample Preparation. Single crystals of $Na_3[Tb(oda)_3]\cdot 2NaClO_4\cdot 6H_2O$ were grown according to the methods of Albertsson.[3,4] Crystals harvested for optical measurements were typically ca. 1−2 mm thick. The crystal samples were attached to copper mounts built for use in the cold head of an optical cryostat. To ensure proper thermal contact, the crystals were mounted using Crycon grease and indium foil at cold-head−crystal interfaces. The crystals were mounted in orientations defined with respect to the alignment of their unique axis relative to the direction of light propagation in the optical absorption experiments and the direction of excitation and emission detection in the optical emission experiments. Parallel alignment of the unique axis and the direction of light propagation is referred to here as an *axial* orientation. Perpendicular alignment of the unique axis and the direction of light propagation is referred to here as an *orthoaxial* orientation.

In our initial optical experiments, the crystal samples were lightly coated with Crycon grease to inhibit their possible deterioration (via efflorescence) under the high-vacuum conditions in the closed-cycle helium refrigerator/cryostat. However, a repeat of these experiments with unprotected crystal samples yielded essentially identical results, and the crystals showed no signs of deterioration during multiple up-and-down temperature changes (between ca. 10 and 293 K) in the cryostat.

Optical Absorption Measurements. Circularly polarized and unpolarized *axial*, and σ and π linearly polarized *orthoaxial* spectra were measured for TbODA. All of the unpolarized axial, and σ and π polarized orthoaxial absorption spectra were obtained with a Cary Model 5 UV−VIS−NIR spectrophotometer. A CTI-cryogenic pump closed-cycle helium refrigerator model 22C controlled by a Lake Shore cryotronics temperature-controller (model DRC-70) was used to achieve cold-head temperatures of either 70 or 20 K. Absorption spectra were recorded over the 235−490 nm wavelength range. The orthoaxial spectral measurements were taken by fitting a linear polarizing element into the spectrophotometer.

Circular dichroism (CD) spectra were measured using instrumentation constructed in our laboratory at the University of Virginia. Broad-band radiation from a xenon arc lamp (500 W, PTI A5000 housing) was used as the excitation source. The excitation light was passed through a linear-polarizing element followed by a Hinds International PEM-80 photoelastic modulator. The polarizer−PEM combination polarizes the excitation light into left and right circularly polarized components. The PEM served as a dynamic polarizer, operating at a modulation frequency of ca. 50 kHz, that alternately transmitted left and right circularly polarized light which was then passed through the sample crystal. The transmitted light was dispersed with a 0.75 m double-grating monochromator, and the transmission intensity was measured using photon-counting techniques. The transmission spectrum was converted to a CD spectrum by correcting for the arc-lamp output profile.

Optical Emission Measurements. Optical emission spectra were measured using instrumentation constructed in our laboratory at the

(15) May, P. S.; Metcalf, D. H.; Richardson, F. S.; Carter, R. C.; Miller, C. E.; Palmer, R. A. *J. Lumin.* **1992**, *51*, 249.
(16) Berry, M. T.; Schwieters, C.; Richardson, F. S. *Chem. Phys.* **1988**, *122*, 105.
(17) Berry, M. T.; Schwieters, C.; Richardson, F. S. *Chem. Phys.* **1988**, *122*, 125.
(18) May, P. S.; Richardson, F. S. *Chem. Phys. Lett.* **1991**, *179*, 277.
(19) Görller-Walrand, C.; Verhoeven, P.; D′Olieslager, J.; Fluyt, L.; Binnemans, K. *J.* Chem. Phys. **1994**, *100*, 815.
(20) Kundu, T.; Banerjee, A. K.; Chowdhury, M. *Phys. Rev. B* **1990**, *41*, 10911.
(21) Stephens, E. M.; Metcalf, D. H.; Berry, M. T.; Richardson, F. S. *Phys. Rev. B* **1991**, *44*, 9895.
(22) Kundu, T.; Banerjee, A. K.; Chowdhury, M. *Chem. Phys.* **1991**, *156*, 95.
(23) Gunde, K. E.; Richardson, F. S. *Chem. Phys.* **1995**, *194*, 195.
(24) Metcalf, D. H.; Hopkins, T. A.; Richardson, F. S. *Inorg. Chem.* **1995**, *34*, 4868.
(25) Moran, D. M.; De Piante, A.; Richardson, F. S. *Phys. Rev. B* **1990**, *42*, 3317.
(26) Moran, D. M.; Richardson, F. S. *Phys. Rev. B* **1990**, *42*, 3331.
(27) Moran, D. M.; Richardson, F. S. *Inorg. Chem.* **1992**, *31*, 813.
(28) Schoene, K. A.; Quagliano, J. R.; Richardson, F. S. *Inorg. Chem.* **1991**, *30*, 3803.
(29) Schoene, K. A. Ph.D. Dissertation, University of Virginia, 1989.
(30) Schwartz, R. W.; Banerjee, A. K.; Sen, A. C.; Chowdhury, M. *J. Chem. Soc., Faraday Trans. 2* **1980**, *76*, 620.
(31) Saxe, J. D.; Morley, J. P.; Richardson, F. S. *Mol. Phys.* **1982**, *47*, 407.
(32) Hammond, R. M. Ph.D. Dissertation, University of Virginia, 1988.
(33) Hopkins, T. A.; Bolender, J. P.; Metcalf, D. H.; Richardson, F. S. *Inorg. Chem.* **1996**, *35*, 5356.

University of Virginia. An argon ion (Ar^+) laser was used as an excitation source; sample luminescence was dispersed with a 0.75 m double-grating monochromator; and luminescence intensity was measured using photon-counting techniques. In all experiments, sample excitation was along the same direction as emission detection. Three different optical cryostats were used to control sample temperature in our emission experiments. A closed-cycle helium refrigerator was used in experiments carried out at 20 and 293 K, and a liquid nitrogen cooled cryostat was used in experiments carried out at 77 K. Single crystals of TbODA were mounted with their unique (optic) axis aligned either parallel or perpendicular to the direction of emission detection. Spectra obtained with the unique axis aligned parallel to the direction of emission detection are referred to as *axial* spectra, whereas those obtained with the unique axis aligned perpendicular to this direction are referred to as *orthoaxial* spectra.

For the trigonal TbODA crystals examined in this study, emission measured along the crystallographic *c* axis (i.e., unique axis), as in our axial measurements, can exhibit at least some degree of circular polarization, and emission measured along a direction that is *perpendicular* to the crystallographic *c* axis (as in our orthoaxial spectral measurements) can exhibit some degree of linear polarization. In our axial emission experiments, the sample luminescence was analyzed in terms of left and right circularly polarized intensity components, while in our orthoaxial emission experiments, the sample luminescence was analyzed in terms of intensity components polarized perpendicular (σ) and parallel (π) to the crystal *c* axis. This was done by using a PEM, operating at a modulation frequency of ca. 100 kHz, that alternately transmitted σ and π polarized luminescence intensities (for the orthoaxial measurements) to the emission detection unit of our spectrophotometer, and by using a PEM-polarizer (inverted order with respect to the CD measurements) combination that alternately transmitted left and right circularly polarized luminescence intensities to the emission detection unit of our spectrophotometer.

All of the luminescence intensity observed in our experiments originates from the $^5D(3)_4$ excited multiplet of Tb^{3+} (centered at ca. 20 480 cm^{-1} above ground). The energy gap between this multiplet and the next lower-energy multiplet ($^7F_0$) is ca. 14700 cm^{-1}, which is larger than any lattice phonon or molecular vibrational energy in TbODA crystals. Therefore, nonradiative decay processes for $^5D(3)_4$ are relatively slow, and this multiplet exhibits a strong luminescence with a high quantum yield. The emission spectra measured in this study include all of the ^7F_J ($J = 0-6$) $\leftarrow$ $^5D(3)_4$ transition regions, spanning the 485−685 nm wavelength range. For the $^7F_{0-5} \leftarrow {}^5D(3)_4$ transition regions, the luminescence was excited with the 488.0 nm line of an argon ion laser, which corresponds to $^7F_6 \leftarrow {}^5D(3)_4$ excitation. The luminescence of the $^7F_6 \leftarrow {}^5D(3)_4$ transition region was excited with UV lines (in the 351−364 nm wavelength range) of an argon ion laser.

Methods of Data Analysis

Optical Selection Rules and Line Assignments. The crystal-field energy levels split out of the $4f^8$ electronic configuration of Tb^{3+} in TbODA may be classified as having A_1, A_2, or E symmetry in the D_3 point group, where A_1, A_2, and E denote irreducible representation (irrep) labels in this group. Therefore, all transitions between crystal-field levels in TbODA may be classified (by symmetry) as $A_1 \leftrightarrow A_1$, $A_2 \leftrightarrow A_2$, $A_1 \leftrightarrow A_2$, $A_1 \leftrightarrow E$, $A_2 \leftrightarrow E$, or $E \leftrightarrow E$. The optical selection rules for each of these transition types depend on the polarization properties of the perturbing radiation and on the interactions responsible for the transitions. All transitions observed in the optical absorption and emission spectra measured in the present study may be presumed to occur via electric and/or magnetic dipole interaction mechanisms, and the relevant interaction operators for connecting crystal-field states are the electric dipole (μ) and magnetic dipole (m) moment operators. Here we express these dipole operators in a spherical coordinate basis, $q = 0, \pm 1$, chosen such that for any given $Tb(oda)_3^{3-}$ complex in TbODA, the $q = 0$ axis is defined to be coincident with the trigonal symmetry axis of the complex and, therefore, parallel to the unique (optic) axis of TbODA. Expressed in this basis, the μ_0 and m_0 components of the μ and m operators each transform as the A_2 irrep under the symmetry operations of the D_3 point group, and the $\mu_{\pm 1}$ and $m_{\pm 1}$ components each transform as the E irrep under the symmetry operations of this group. Given these symmetry properties of the μ_q and m_q operator components, electric and magnetic dipole selection rules are easily derived for each of the six transition types defined above. The selection rules relevant to the optical absorption and emission measurements performed on TbODA are shown in Table 1.

Table 1. Electric (μ) and Magnetic (m) Dipole Selection Rules for Optical Absorption and Emission Measurements on $Tb(oda)_3^{3-}$ Complexes in Trigonal $Na_3[Tb(oda)_3]\cdot 2NaClO_4\cdot 6H_2O$ Crystals

transition type[a]	axial spectra[b]	orthoaxial spectra[c]	
		σ polarized	π polarized
$A_1 \leftrightarrow A_1$	forbidden	forbidden	forbidden
$A_1 \leftrightarrow A_2$	forbidden	m_0	μ_0
$A_2 \leftrightarrow A_2$	forbidden	forbidden	forbidden
$A_1 \leftrightarrow E$	$\mu_{\pm 1}$; $m_{\pm 1}$	$\mu_{\pm 1}$	$m_{\pm 1}$
$A_2 \leftrightarrow E$	$\mu_{\pm 1}$; $m_{\pm 1}$	$\mu_{\pm 1}$	$m_{\pm 1}$
$E \leftrightarrow E$	$\mu_{\pm 1}$; $m_{\pm 1}$	$\mu_{\pm 1}$; m_0	μ_0; $m_{\pm 1}$

[a] Energy levels are labeled according to their irreducible representation (irrep) in the D_3 point group. [b] Light propagating along the crystallographic *c* axis (the *unique* axis), which is parallel to the trigonal symmetry axes of the $Tb(oda)_3^{3-}$ complexes. [c] Light propagating along a direction perpendicular to the crystallographic *c* axis.

Nearly all of the transitions observed in the absorption spectra measured in this study are predicted, either by direct calculation or by application of ΔJ, ΔL, and ΔS selection rules, to occur via predominantly *electric dipole* interaction mechanisms. Therefore, assignments of these transitions, with respect to symmetry type, could be made relatively unambiguously by applying the electric dipole selection rules of Table 1 to the combination of results obtained from our axial and polarized orthoaxial absorption intensity measurements. Similarly, the transitions observed in the $^5D(3)_4 \rightarrow {}^7F_6$, $^7F_2$, $^7F_1$, and $^7F_0$ emission regions of Tb^{3+} in TbODA are also expected to have predominantly electric dipole character and, therefore, be amenable to unambiguous symmetry assignment. However, the situation is somewhat different in the $^5D(3)_4 \rightarrow {}^7F_5$, $^7F_4$, and $^7F_3$ emission regions, where many of the transitions are expected to exhibit line intensity and polarization properties that reflect both electric and magnetic dipole interaction mechanisms. Line assignments in these emission regions could not be based solely on applications of the selection rules given in Table 1, but they were aided by results obtained from *direct* calculations of magnetic dipole transition line strengths.

We note from Table 1 that the only transition types observable in our *axial* absorption and emission spectra measurements are those in which at least one of the connecting levels has E symmetry. These are the only transition types that appear in the circular dichroism (CD) and circularly polarized luminescence (CPL) spectra measured in this study.

Energy Level Analysis. The $4f^8$ electronic energy-level structure of Tb^{3+} in TbODA was analyzed in terms of a model Hamiltonian that is fully commensurate with the model Hamiltonian employed previously in our studies of other LnODA systems.[8,12,16,21,24,25,28] It will be convenient for our discussions here to partition this Hamiltonian as follows:

$$\hat{H} = \hat{H}_a + \hat{H}_{cf}^+ \qquad (1)$$

where $\hat{H}_a$ is defined to incorporate the isotropic, *atomic-like* parts of $\hat{H}$ (including the spherically symmetric parts of the 4f electron/crystal-field interactions) and $\hat{H}_{cf}^+$ is defined to represent the nonspherically symmetric components of the *even-parity* crystal field. We will refer to $\hat{H}_a$ as the *atomic* Hamiltonian and will call $\hat{H}_{cf}^+$ the *crystal-field* Hamiltonian. Both the $\hat{H}_a$ and $\hat{H}_{cf}^+$ parts of the model Hamiltonian are defined to operate entirely *within* the $4f^8(Tb^{3+})$ electronic configuration; however, $\hat{H}_a$ contains a number of "effective" two- and three-body interaction terms parametrized to include implicit consideration of interconfigurational mixings between $4f^8$ and higher-energy configurations of like parity.

Table 2. Calculated and Experimentally Observed Crystal-field Energy Levels of Tb^{3+} in $Na_3[Tb(oda)_3]\cdot 2NaClO_4\cdot 6H_2O$

				energy (cm^{-1})							energy (cm^{-1})		
level no.	term[a]	J[a]	Γ[b]	calc[c]	expt[d]	Δ[e]	level no.	term[a]	J[a]	Γ[b]	calc[c]	expt[d]	Δ[e]
1	^7F	6	A_1	−9	0	−9	68	^5G (3)	5	E	27 741	27 741	0
2	^7F	6	E	9	6	3	69	^5G (3)	5	E	27 756	27 761	−5
3	^7F	6	A_2	21	18	3	70	^5G (3)	5	A_2	27 757	n.d.	
4	^7F	6	A_1	22	30	−8	71	^5G (3)	5	A_1	27 760	n.d.	
5	^7F	6	E	50	68	−18	72	^5G (3)	5	E	27 774	n.d.	
6	^7F	6	A_2	166	n.d.		73	^5G (3)	5	E	27 823	27 832	−9
7	^7F	6	E	172	n.d.		74	^5G (3)	5	A_2	27 851	n.d.	
8	^7F	6	A_1	176	n.d.		75	^5D (3)	2	A_1	28 121	n.d.	
9	^7F	6	E	196	n.d.		76	^5D (3)	2	E	28 141	28 139	2
10	^7F	5	A_1	2 013	2 047	−34	77	^5D (3)	2	E	28 154	n.d.	
11	^7F	5	A_2	2 043	2 062	−19	78	^5G (2)	4	A_1	28 218	n.d.	
12	^7F	5	E	2 061	2 078	−17	79	^5G (2)	4	E	28 218	28 233	−15
13	^7F	5	E	2 109	2 111	−2	80	^5G (2)	4	A_2	28 228	n.d.	
14	^7F	5	E	2 148	2 146	2	81	^5G (2)	4	A_1	28 252	n.d.	
15	^7F	5	E	2 257	n.d.		82	^5G (2)	4	E	28 260	n.d.	
16	^7F	5	A_2	2 301	2 292	9	83	^5G (2)	4	E	28 281	n.d.	
17	^7F	4	A_1	3 225	n.d.		84	^5L	9	A_2	28 315	n.d.	
18	^7F	4	E	3 313	3 320	−7	85	^5L	9	E	28 332	n.d.	
19	^7F	4	A_2	3 376	3 376	0	86	^5L	9	E	28 373	n.d.	
20	^7F	4	A_1	3 415	3 398	17	87	^5L	9	A_1	28 388	n.d.	
21	^7F	4	E	3 415	3 406	9	88	^5L	9	E	28 425	n.d.	
22	^7F	4	E	3 596	3 621	−25	89	^5L	9	A_2	28 454	n.d.	
23	^7F	3	E	4 343	4 326	19	90	^5L	9	A_1	28 456	n.d.	
24	^7F	3	A_1	4 376	4 345	31	91	^5L	9	E	28 465	28 478	−13
25	^7F	3	E	4 401	4 405	−4	92	^5L	9	E	28 517	n.d.	
26	^7F	3	A_2	4 408	4 414	−6	93	^5L	9	A_2	28 540	n.d.	
27	^7F	3	A_2	4 459	4 468	−9	94	^5L	9	A_1	28 549	n.d.	
28	^7F	2	A_1	5 015	4 992	23	95	^5L	9	E	28 565	28 559	6
29	^7F	2	E	5 056	5 055	1	96	^5L	9	A_2	28 587	28 609	−22
30	^7F	2	E	5 159	5 157	2	97	^5G (2)	3	A_2	28 901	n.d.	
31	^7F	1	A_2	5 532	5 517	15	98	^5G (2)	3	E	28 912	28 905	7
32	^7F	1	E	5 540	5 534	6	99	^5G (2)	3	A_2	28 933	28 936	−3
33	^7F	0	A_1	5 756	5 750	6	100	^5G (2)	3	A_1	28 946	n.d.	
34	^5D (3)	4	E	20 468	20 462	6	101	^5G (2)	3	E	28 948	28 957	−9
35	^5D (3)	4	A_1	20 444	n.d.		102	^5L	8	E	29 082	n.d.	
36	^5D (3)	4	A_2	20 467	20 468	−1	103	^5L	8	A_1	29 099	n.d.	
37	^5D (3)	4	E	20 483	20 475	8	104	^5L	8	E	29 108	29 106	2
38	^5D (3)	4	A_1	20 509	20 493	16	105	^5L	8	A_2	29 131	29 126	5
39	^5D (3)	4	E	20 527	20 512	15	106	^5L	8	A_2	29 151	29 148	3
40	^5D (3)	3	A_2	26 143	26 147	−4	107	^5L	8	A_1	29 155	n.d.	
41	^5D (3)	3	E	26 207	26 195	12	108	^5L	8	E	29 173	29 179	−6
42	^5D (3)	3	A_1	26 213	n.d.		109	^5L	8	E	29 200	n.d.	
43	^5D (3)	3	E	26 234	26 219	15	110	^5L	8	E	29 257	29 249	8
44	^5D (3)	3	A_2	26 246	26 265	−19	111	^5L	8	E	29 271	n.d.	
45	^5G (3)	6	A_1	26 328	n.d.		112	^5L	8	A_1	29 290	n.d.	
46	^5G (3)	6	E	26 386	26 381	5	113	^5L	7	E	29 317	n.d.	
47	^5G (3)	6	A_2	26 416	n.d.		114	^5G (2)	2	A_1	29 347	n.d.	
48	^5G (3)	6	A_1	26 426	n.d.		115	^5L	7	E	29 363	29 377	−14
49	^5G (3)	6	E	26 434	26 429	5	116	^5L	7	A_2	29 378	n.d.	
50	^5G (3)	6	A_2	26 442	n.d.		117	^5L	8	A_1	29 403	n.d.	
51	^5G (3)	6	E	26 459	n.d.		118	^5G (2)	2	E	29 407	29 410	−3
52	^5G (3)	6	A_1	26 536	n.d.		119	^5L	7	A_2	29 419	n.d.	
53	^5G (3)	6	E	26 552	26 535	17	120	^5G (2)	2	E	29 447	n.d.	
54	^5L	10	E	26 825	26 817	8	121	^5L	7	E	29 471	29 464	7
55	^5L	10	A_2	26 825	n.d.		122	^5L	7	E	29 503	n.d.	
56	^5L	10	E	26 847	26 840	7	123	^5L	7	A_2	29 533	n.d.	
57	^5L	10	A_1	26 863	n.d.		124	^5L	7	A_1	29 570	n.d.	
58	^5L	10	E	27 005	n.d.		125	^5L	6	A_1	29 590	n.d.	
59	^5L	10	E	27 027	n.d.		126	^5L	7	E	29 592	n.d.	
60	^5L	10	A_2	27 068	n.d.		127	^5L	6	E	29 612	n.d.	
61	^5L	10	A_1	27 086	n.d.		128	^5L	7	A_2	29 646	n.d.	
62	^5L	10	A_2	27 094	n.d.		129	^5L	6	E	29 729	n.d.	
63	^5L	10	A_1	27 096	n.d.		130	^5L	6	E	29 747	n.d.	
64	^5L	10	E	27 152	n.d.		131	^5L	6	A_2	29 748	n.d.	
65	^5L	10	E	27 163	n.d.		132	^5L	6	A_1	29 771	n.d.	
66	^5L	10	E	27 214	n.d.		133	^5L	6	E	29 861	n.d.	
67	^5L	10	A_1	27 234	n.d.		134	^5L	6	A_1	29 891	n.d.	

Table 2 (Continued)

level no.	term[a]	J[a]	Γ[b]	energy (cm^{-1}) calc[c]	expt[d]	Δ[e]	level no.	term[a]	J[a]	Γ[b]	energy (cm^{-1}) calc[c]	expt[d]	Δ[e]
135	^{5}D (3)	1	E	30 659	30 653	6	204	^{5}I (2)	7	E	36 573	n.d.	
136	^{5}D (3)	1	A_2	30 668	30 671	−3	205	^{5}I (2)	7	A_2	36 575	36 566	9
137	^{5}H (1)	7	A_2	31 268	31 249	19	206	^{5}I (2)	7	A_1	36 582	n.d.	
138	^{5}D (3)	0	A_1	31 283	n.d.		207	^{5}I (2)	7	E	36 583	36 579	4
139	^{5}H (1)	7	E	31 287	n.d.		208	^{5}I (2)	7	E	36 587	n.d.	
140	^{5}H (1)	7	E	31 346	31 345	1	209	^{5}I (2)	7	A_2	36 592	n.d.	
141	^{5}H (1)	7	E	31 355	n.d.		210	^{5}I (2)	7	E	36 610	n.d.	
142	^{5}H (1)	7	A_2	31 363	31 364	−1	211	^{5}I (2)	7	A_1	36 611	n.d.	
143	^{5}H (1)	7	A_1	31 366	n.d.		212	^{5}I (2)	7	E	36 620	n.d.	
144	^{5}H (1)	7	A_2	31 444	31 442	2	213	^{5}I (2)	7	A_2	36 658	n.d.	
145	^{5}H (1)	7	A_1	31 453	n.d.		214	^{5}F (2)	2	E	37 052	n.d.	
146	^{5}H (1)	7	E	31 456	n.d.		215	^{5}F (2)	2	E	37 074	n.d.	
147	^{5}H (1)	7	E	31 471	31 477	−6	216	^{5}F (2)	2	A_1	37 079	n.d.	
148	^{5}H (1)	6	A_1	32 766	n.d.		217	^{5}F (2)	1	E	37 350	n.d.	
149	^{5}H (1)	6	E	32 796	n.d.		218	^{5}F (2)	1	A_2	37 358	n.d.	
150	^{5}H (1)	6	E	32 851	32 848	3	219	^{5}I (2)	4	E	37 476	n.d.	
151	^{5}H (1)	6	A_2	32 864	32 860	4	220	^{5}I (2)	4	A_2	37 511	n.d.	
152	^{5}H (1)	6	A_1	32 893	n.d.		221	^{5}I (2)	6	E	37 537	n.d.	
153	^{5}H (1)	6	E	32 911	32 922	−11	222	^{5}I (2)	6	A_1	37 554	n.d.	
154	^{5}H (1)	6	A_1	32 940	n.d.		223	^{5}I (2)	6	A_1	37 567	n.d.	
155	^{5}H (1)	6	E	32 950	32 964	−14	224	^{5}I (2)	4	E	37 575	37 580	−5
156	^{5}H (1)	6	A_2	32 982	32 983	−1	225	^{5}I (2)	6	A_1	37 585	n.d.	
157	^{5}H (1)	5	A_2	33 670	n.d.		226	^{5}I (2)	6	E	37 590	n.d.	
158	^{5}H (1)	5	E	33 690	33 690	0	227	^{5}I (2)	6	E	37 605	n.d.	
159	^{5}H (1)	5	E	33 745	n.d.		228	^{5}I (2)	6	A_1	37 612	n.d.	
160	^{5}H (1)	5	E	33 762	n.d.		229	^{5}I (2)	6	A_2	37 617	n.d.	
161	^{5}H (1)	5	E	33 780	33 788	−8	230	^{5}I (2)	6	E	37 636	n.d.	
162	^{5}H (1)	5	A_2	33 781	n.d.		231	^{5}I (2)	6	A_2	37 669	n.d.	
163	^{5}H (1)	5	A_1	33 799	n.d.		232	^{5}I (2)	4	E	37 677	n.d.	
164	^{5}H (1)	4	E	34 271	n.d.		233	^{5}I (2)	4	A_1	37 719	n.d.	
165	^{5}H (1)	4	A_1	34 285	n.d.		234	^{5}I (2)	5	A_2	37 965	n.d.	
166	^{5}H (1)	4	E	34 321	n.d.		235	^{5}I (2)	5	E	37 966	n.d.	
167	^{5}H (1)	4	A_2	34 322	n.d.		236	^{5}I (2)	5	A_1	37 969	n.d.	
168	^{5}H (1)	4	E	34 331	n.d.		237	^{5}I (2)	5	E	37 986	n.d.	
169	^{5}H (1)	4	A_1	34 342	n.d.		238	^{5}I (2)	5	A_2	37 998	n.d.	
170	^{5}H (1)	3	A_2	34 807	n.d.		239	^{5}I (2)	5	E	38 005	n.d.	
171	^{5}F (2)	5	E	34 822	34 809	13	240	^{5}I (2)	5	E	38 010	n.d.	
172	^{5}F (2)	5	A_2	34 844	34 846	−1	241	^{5}K	9	A_2	39 009	38 990	19
173	^{5}F (2)	5	E	34 851	n.d.		242	^{5}K	9	E	39 023	39 027	−4
174	^{5}F (2)	5	A_2	34 897	n.d.		243	^{5}K	9	E	39 050	n.d.	
175	^{5}H (1)	3	E	34 904	n.d.		244	^{5}K	9	A_2	39 070	n.d.	
176	^{5}F (2)	5	E	34 911	n.d.		245	^{5}K	9	A_1	39 082	n.d.	
177	^{5}F (2)	5	A_2	34 942	n.d.		246	^{5}K	9	E	39 130	n.d.	
178	^{5}H (1)	3	A_1	34 946	n.d.		247	^{5}K	9	E	39 151	n.d.	
179	^{5}F (2)	5	A_1	34 949	n.d.		248	^{5}K	9	A_2	39 163	n.d.	
180	^{5}H (1)	3	E	34 968	n.d.		249	^{5}K	9	A_1	39 199	n.d.	
181	^{5}H (1)	3	E	35 033	35 031	2	250	^{5}K	9	E	39 255	n.d.	
182	^{5}I (2)	8	E	35 048	35 046	2	251	^{5}K	9	A_1	39 257	n.d.	
183	^{5}I (2)	8	E	35 059	n.d.		252	^{5}K	9	A_2	39 266	n.d.	
184	^{5}I (2)	8	A_2	35 063	n.d.		253	^{5}K	9	E	39 269	n.d.	
185	^{5}I (2)	8	A_1	35 097	n.d.		254	^{5}D (2)	2	A_1	39 318	n.d.	
186	^{5}I (2)	8	E	35 113	35 107	6	255	^{5}D (2)	2	E	39 319	39 346	−27
187	^{5}I (2)	8	E	35 136	n.d.		256	^{5}D (2)	2	E	39 337	39 368	−31
188	^{5}I (2)	8	A_2	35 139	n.d.		257	^{5}K	6	A_2	40 048	n.d.	
189	^{5}I (2)	8	A_1	35 142	n.d.		258	^{5}K	6	E	40 098	n.d.	
190	^{5}I (2)	8	E	35 179	n.d.		259	^{5}K	6	A_1	40 102	n.d.	
191	^{5}I (2)	8	E	35 187	35 186	1	260	^{5}K	6	E	40 129	n.d.	
192	^{5}I (2)	8	A_1	35 196	n.d.		261	^{5}K	6	A_1	40 146	n.d.	
193	^{5}F (2)	4	E	35 334	35 338	−4	262	^{5}K	6	A_2	40 177	n.d.	
194	^{5}F (2)	4	A_1	35 335	n.d.		263	^{5}K	6	E	40 182	n.d.	
195	^{5}F (2)	4	E	35 371	35 366	5	264	^{5}K	6	E	40 246	n.d.	
196	^{5}F (2)	4	E	35 389	n.d.		265	^{5}K	6	A_1	40 291	n.d.	
197	^{5}F (2)	4	A_2	35 392	n.d.		266	^{5}K	8	A_1	40 674	n.d.	
198	^{5}F (2)	4	A_1	35 411	n.d.		267	^{5}K	8	E	40 694	n.d.	
199	^{5}F (2)	3	A_1	36 411	n.d.		268	^{5}K	8	E	40 713	n.d.	
200	^{5}F (2)	3	A_2	36 436	n.d.		269	^{5}K	8	E	40 731	n.d.	
201	^{5}F (2)	3	E	36 458	n.d.		270	^{5}K	8	A_2	40 748	n.d.	
202	^{5}F (2)	3	A_2	36 478	n.d.		271	^{5}K	8	A_1	40 755	n.d.	
203	^{5}F (2)	3	E	36 494	36 494	0	272	^{5}K	8	E	40 758	n.d.	

Table 2 (Continued)

level no.	term[a]	J[a]	Γ[b]	energy (cm^{-1}) calc[c]	expt[d]	Δ[e]	level no.	term[a]	J[a]	Γ[b]	energy (cm^{-1}) calc[c]	expt[d]	Δ[e]
273	^{5}K	8	E	40 821	n.d.		293	^{5}K	7	E	41 574	n.d.	
274	^{5}K	8	A_2	40 822	n.d.		294	^{5}K	7	A_2	41 600	n.d.	
275	^{5}K	8	E	40 831	n.d.		295	^{5}K	7	E	41 605	n.d.	
276	^{5}K	8	A_1	40 842	n.d.		296	^{5}K	7	A_1	41 619	n.d.	
277	^{5}G (2)	6	E	41 200	n.d.		297	^{5}K	7	A_2	41 624	n.d.	
278	^{5}G (2)	6	E	41 211	n.d.		298	^{5}K	7	E	41 632	n.d.	
279	^{5}K	5	A_2	41 220	n.d.		299	^{5}K	7	E	41 680	n.d.	
280	^{5}K	5	E	41 231	41 235	−4	300	^{5}K	7	A_1	41 693	n.d.	
281	^{5}G (2)	6	A_1	41 236	n.d.		301	^{5}K	7	A_2	41 695	n.d.	
282	^{5}K	5	E	41 258	n.d.		302	^{5}K	7	E	41 699	n.d.	
283	^{5}K	5	A_1	41 283	n.d.		303	^{5}D (2)	3	A_2	42 003	n.d.	
284	^{5}K	5	E	41 284	n.d.		304	^{5}D (2)	3	A_1	42 075	n.d.	
285	^{5}K	5	A_2	41 285	n.d.		305	^{5}D (2)	3	E	42 078	n.d.	
286	^{5}K	5	A_2	41 306	n.d.		306	^{5}D (2)	3	A_2	42 119	42 102	17
287	^{5}K	5	E	41 315	n.d.		307	^{5}D (2)	3	E	42 142	n.d.	
288	^{5}K	5	A_1	41 338	n.d.		308	^{5}G (2)	5	E	42 319	42 303	16
289	^{5}K	5	E	41 361	n.d.		309	^{5}G (2)	5	A_2	42 322	n.d.	
290	^{5}K	5	A_2	41 369	n.d.		310	^{5}G (2)	5	E	42 329	n.d.	
291	^{5}K	5	E	41 370	n.d.		311	^{5}G (2)	5	E	42 359	42 353	6
292	^{5}K	5	A_1	41 372	n.d.		312	^{5}G (2)	5	A_2	42 371	n.d.	
							313	^{5}G (2)	5	A_1	42 372	n.d.	
							314	^{5}G (2)	5	E	42 386	n.d.	

[a] Identifies the *principal* SLJ components of the eigenvectors. [b] Irreducible representation (irrep) label in D_3 point group. [c] Calculated by using the Hamiltonian parameter values listed in Table 3. [d] Experimentally determined locations of energy levels, with $1/\lambda$(air) to $1/\lambda$(vacuum) corrections included. Uncertainties in the energy−level locations are ca. ±3 cm^{-1} (on average). n.d. ≡ not determined (i.e., energy level not fully characterized with respect to location and/or symmetry type). [e] Difference between calculated and observed energies.

Table 3. Energy Parameters for the 4f^8 Electronic Configuration of Tb^{3+} in $Na_3[Tb(oda)_3]\cdot 2NaClO_4\cdot 6H_2O$

parameter[a]	value[b]/cm^{-1}	parameter[a]	value[b]/cm^{-1}
E_{av}	68 195(7)	M^0	1.95(0.07)
F^2	90 251(25)	M^2	$0.56M^0$
F^4	64 414(48)	M^4	$0.38M^0$
F^6	43 627(53)	P^2	[373]
ζ_{so}	1700(2)	P^4	[186]
α	18.6(0.1)	P^6	[37]
β	−643(17)	B_0^2	51(41)
γ	[1652]	B_0^4	−955(57)
T^2	[320]	B_3^4	−791(41)
T^3	[40]	B_0^6	−664(90)
T^4	[50]	B_3^6	−1048(57)
T^6	[−395]	B_6^6	−877(51)
T^7	[303]		
T^8	[317]	N^c	95
		σ^d	11.7

[a] Defined according to eqs 2 and 4. [b] Determined from parametric fits of the experimentally observed energy-level data listed in Table 2. The numbers shown in parentheses represent uncertainties in the parameter values and correspond to the (±) changes in parameter values that produce a doubling of the *variance* obtained in the data fits. The parameter values shown in square brackets were held fixed in performing the data fits. [c] Number of assigned energy levels included in the parametric data fits. [d] Root-mean-square deviation between calculated and observed energies (in cm^{-1}).

The atomic Hamiltonian used in the present study may be written in the following parametrized form:

$$\hat{H}_a = E_{av} + \sum_k F^k \hat{f}_k + \alpha \hat{L}(\hat{L}+1) + \beta \hat{G}(G_2) + \gamma \hat{G}(R_7) + \sum_i T^i \hat{t}_i + \zeta_{so} \hat{A}_{so} + \sum_k P^k \hat{p}_k + \sum_j M^j \hat{m}_j \quad (2)$$

where $k = 2, 4, 6$; $i = 2, 3, 4, 6, 7, 8$; $j = 0, 2, 4$; and each of the interaction operators and parameters is written and defined according to conventional practice.[34,35] Defined according to eq 2, the $\hat{H}_a$ operator contains 20 parameters (including E_{av}). Implicit in these parameters are the radial-coordinate-dependent parts of the interactions represented in $\hat{H}_a$.

Table 4. Comparisons of Crystal-Field Parameters and Interaction Strengths Reported for Tb^{3+} in Three Crystal Systems Having *Trigonal* Site Symmetries[a]

parameter[b]	TbODA (D_3)[c]	$Yb_{0.95}Tb_{0.05}DPA$ (D_3)[d]	Tb^{3+}:$LaCl_3$ (C_{3h})[e]
B_0^2	51	−140	184
B_0^4	−955	−325	−295
B_3^4	−791	−365	
B_0^6	−664	−610	−459
B_3^6	−1048	−611	
B_6^6	−877	−898	284
S_{cf}^2	23	63	82
S_{cf}^4	490	203	98
S_{cf}^6	567	458	169
S_{cf}	433	292	122

[a] All parameter values are given in units of cm^{-1}. [b] The B_m^k crystal-field parameters are defined according to eq 3 in text. The S_{cf}^k and S_{cf} crystal-field *strength* parameters are defined according to eqs 5 and 6 in the text. [c] From present work. [d] From ref 33. [e] From ref 38.

The even-parity crystal-field Hamiltonian, $\hat{H}_{cf}^+$, is defined to reflect the D_3 point symmetry at the Tb^{3+} sites in TbODA and is expressed here as

$$\hat{H}_{cf} = \sum_{k,m} B_m^k \hat{C}_m^{(k)} \quad (3)$$

where $k = 2, 4, 6$; $m = 0, \pm 3, \pm 6$ (with $|m| \le k$); $\hat{C}_m^{(k)}$ is a many-electron spherical-tensor operator (of rank k and order m) that acts within the 4f^8(Tb^{3+}) electronic configuration; and the B_m^k are crystal-field interaction parameters. The B_m^k parameters in eq 3 are interrelated according to $B_{-m}^k = (-1)^m B_m^k$, and, therefore, the $\hat{H}_{cf}^+$ operator may be reexpressed as

(34) Crosswhite, H. M.; Crosswhite, H. *J. Opt. Soc. Am. B* **1984**, *1*, 246.
(35) Carnall, W. T.; Goodman, G. L.; Rajnak, K.; Rana, R. S. *J. Chem. Phys.* **1989**, *90*, 3443.

Table 5. Comparisons of Crystal-Field Parameters and Interaction Strengths Determined for Eight $Na_3[Ln(oda)_3]\cdot 2NaClO_4\cdot 6H_2O$ Systems[a]

	values/cm^{-1}							
parameter[b]	NdODA[c]	SmODA[d]	EuODA[e]	GdODA[f]	TbODA[g]	DyODA[h]	HoODA[i]	ErODA[j]
B_0^2	−41(20)	13(26)	67(43)	63(10)	51(41)	59(13)	64(23)	65(31)
B_0^4	−985(53)	−834(44)	−839(60)	−844(32)	−955(57)	−755(25)	−741(38)	−781(69)
B_3^4	−836(32)	−742(27)	−692(41)	−749(12)	−791(41)	−588(21)	−512(28)	−660(50)
B_0^6	−452(59)	−474(42)	−322(61)	−629(265)	−664(90)	−393(27)	−416(48)	−293(49)
B_3^6	−1063(41)	−871(31)	−810(53)	−937(81)	−1048(57)	−620(17)	−608(31)	−517(38)
B_6^6	−694(53)	−622(34)	−591(57)	−752(19)	−877(51)	−581(16)	−526(31)	−507(29)
S_{cf}^2	18(9)	6(12)	30(19)	28(4)	23(18)	26(6)	29(10)	29(14)
S_{cf}^4	513(16)	447(14)	430(20)	451(8)	490(19)	374(9)	345(13)	406(23)
S_{cf}^6	513(18)	440(12)	403(21)	503(35)	567(22)	351(7)	336(12)	296(13)
S_{cf}	419(29)	362(23)	341(35)	390(46)	433(36)	297(14)	279(22)	291(35)
N	116	144	61	60	95	152	105	65
σ	14.4	12.3	9.9	6.3	11.7	8.2	9.1	9.6

[a] Determined from parametric analyses of empirical energy-level data. N = number of assigned energy levels included in the data fits. σ = rms deviation between calculated and observed energies (expressed in cm^{-1}). [b] The B_m^k crystal-field parameters are defined according to eq 4 in the text. The S_{cf}^k and S_{cf} are defined according to eqs 5 and 6 in the text. [c] From ref 8. [d] From ref 12. [e] From ref 16. and J. Quagliano (University of Virginia), unpublished results. [f] From ref 21. [g] From present work. [h] From ref 24. [i] From ref 25. [j] From ref 28.

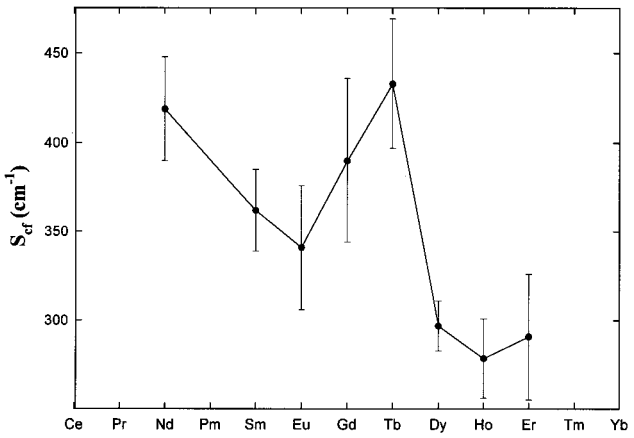

Figure 1. Plot of the crystal-field interaction strength (S_{cf}) quantities determined for eight LnODA systems. Connecting lines between adjacent points are included for clarity.

$$\hat{H}_{cf}^{+} = B_0^2\hat{C}_0^{(2)} + B_0^4\hat{C}_0^{(4)} + B_3^4(\hat{C}_3^{(4)} - \hat{C}_{-3}^{(4)}) + B_0^6\hat{C}_0^{(6)} + B_3^6(\hat{C}_3^{(6)} - \hat{C}_{-3}^{(6)}) + B_6^6(\hat{C}_6^{(6)} + \hat{C}_{-6}^{(6)}) \quad (4)$$

which contains just six independent crystal-field interaction parameters.

Our energy-level calculations were carried out in two steps. In the first step the atomic Hamiltonian was diagonalized within the *complete* set of $f^8SM_SLM_L$ angular-momentum states with the parameters of $\hat{H}_a$ fixed at the values reported previously for Tb^{3+} in LaF_3.[35] The 740 lowest-energy $f^8[SL]JM_J$ intermediate-coupled states derived from this calculation were then used as the basis set in our calculations of crystal-field energy-level structure. In these latter calculations, the *complete* model Hamiltonian ($\hat{H} = \hat{H}_a + \hat{H}_{cf}^{+}$) was diagonalized within the f^8-$[SL]JM_J$ basis with 14 of the 26 parameters in our model Hamiltonian ($\hat{H} = \hat{H}_a + \hat{H}_{cf}^{+}$) treated as variables to fit calculated energy levels to experimentally observed energy-level data. The parameters treated as variables in the calculations included all six B_m^k crystal-field parameters and 8 of the 20 *atomic* Hamiltonian parameters (E_{av}, $F^{2,4,6}$, α, β, ζ_{so}, M^0). The T^i ($i = 2, 3, 4, 6, 7, 8$), γ, and $P^{2,4,6}$ parameters were assigned fixed values taken from a previous analysis of $4f^8(Tb^{3+})$ in LaF_3.[35] The M^2 and M^4 parameters were constrained according to the following relationships: $M^2 = 0.56M^0$ and $M^4 = 0.38M^0$, with M^0 treated as a free variable in performing the data fits. Both the energies and symmetries of crystal-field levels were considered in performing these parametric data fits.

Results and Discussion

Energy Levels. The energy levels located and assigned from our optical and chiroptical measurements on TbODA are shown in Table 2, along with a listing of all calculated energy levels between 0 and 42 400 cm^{-1}. The levels are characterized with respect to their principal ^{2S+1}L term and J multiplet parentages, their crystal-field symmetry label ($\Gamma \equiv A_1$, A_2, or E) in the D_3 point group, and their observed and/or calculated energies. The calculated levels listed in Table 2 were obtained using the Hamiltonian parameter values shown in Table 3. The latter were derived from parametric fits of calculated-to-observed energy-level data. The number of observed levels included in these data fits was 95, and the number of Hamiltonian parameters allowed to freely vary in performing the final data fits was 14.

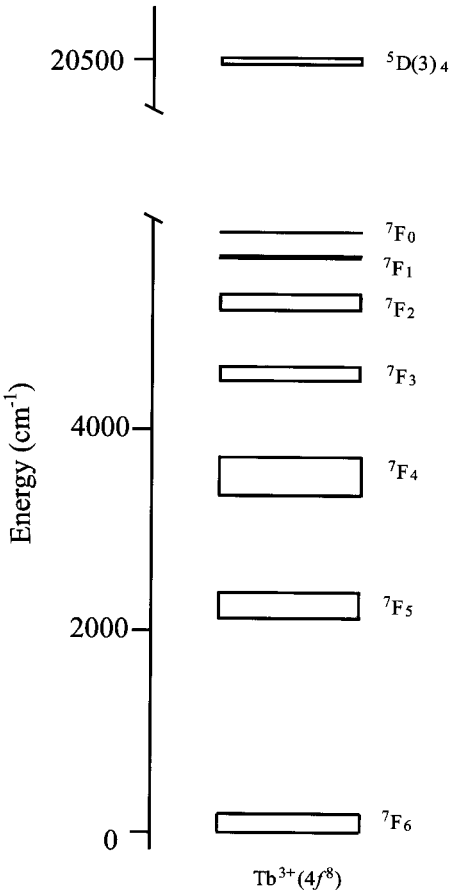

Figure 2. Energy diagram showing the locations and widths of the eight lowest-energy $4f^8[SL]J$ multiplet manifolds of Tb^{3+} in TbODA. See Table 2 for greater detail.

The parameter values shown inside square brackets in the Table 3 listing were held fixed in carrying out the final data fits. The empirical data set was too small and spanned too few of the $^{2S+1}L_J$ multiplet manifolds to permit a more thorough exploration of the overall atomic Hamiltonian parameter space.

The 95 experimental levels listed in Table 2 span the 46 lowest-energy $^{2S+1}L_J$ multiplet manifolds of $4f^8(Tb^{3+})$. Many more of the 314 levels falling within the spectral range of our measurements (0−42 550 cm^{-1}) were located but could not be unambiguously characterized with respect to symmetry. Only the 95 fully assigned levels were used in our energy-level data fits. The root-mean-square (rms) deviation between the calculated and observed energies of these 95 assigned levels is 11.7 cm^{-1}. The overall quality of the energy-level data fit is reasonably good, particularly for an electronic state structure as complex as that of $4f^8(Tb^{3+})$ in TbODA. However, an unresolved problem remains in the calculated orderings of the three lowest crystal-field levels split out of the $^5D(3)_4$ multiplet, and our fits of the energy-level structures observed within several of the ^7F_J multiplet manifolds show rms deviations >13 cm^{-1} (but in all cases <18 cm^{-1}). All attempts to fix these problems by making surgical adjustments in selected parameters of the model Hamiltonian either failed to resolve the problems or led to a significant degradation in the quality of the *overall* data fits. The discrepancies between calculated and experimentally observed energy-level orderings in $^5D(3)_4$ are especially troublesome because each of the levels in question may be expected to make contributions to the emission spectra measured in this study. Our calculations show the following locations and symmetry assignments for the three lowest crystal-field levels of $^5D(3)_4$: an A_1 level at 20 444 cm^{-1}; an A_2 level at 20 467 cm^{-1}; and an E level at 20 468 cm^{-1}. However, both our absorption and emission spectra measurements indicate that an E level lies lowest (at 20 462 cm^{-1}) and an A_2 level is located at 20 468 cm^{-1}, but these measurements fail to locate the predicted low-lying A_1 level. It is possible, of course, that this A_1 level does in fact lie lowest in energy but does not participate in any optical transitions detectable in our experiments.

Comparisons of Crystal Field Parameters and Interaction Strengths. In Table 4 we show a comparison of the crystal-field interaction parameters (B_m^k) determined for $Tb^{3+}(4f^8)$ in three different trigonally symmetric systems (including TbODA), and in Table 5 we show a comparison of the crystal-field interaction parameters determined for eight different LnODA systems. All of the B_m^k parameters given in these tables are defined according to eq 3, with spherical tensor normalization properties. Note, however, that the B_3^4 and B_3^6 parameters vanish in the C_{3h} site symmetry of Tb^{3+} in $LaCl_3$.

Also shown in Tables 4 and 5 are comparisons of the *crystal-field interaction strength* quantities, S_{cf}^k and S_{cf}, determined for the various systems. These quantities are defined in terms of the B_m^k interaction parameters according to

$$S_{cf}^{\ k} = \left(\frac{1}{2k+1}[(B_0^{\ k})^2 + 2\sum_{m>0}|B_m^{\ k}|^2]\right)^{1/2} \quad (5)$$

$$S_{cf} = \left[\frac{1}{3}\sum_k (S_{cf}^{\ k})^2\right]^{1/2} \quad (6)$$

These interaction strength quantities provide a measure of the extent to which the nonspherically symmetric components of the crystal-field interactions induce J level mixings and shift the baricenter energies of J multiplet manifolds.[36,37] They are frequently used for comparisons of the relative strengths of Ln^{3+}-$(4f^N)$/crystal-field interactions in different host materials.

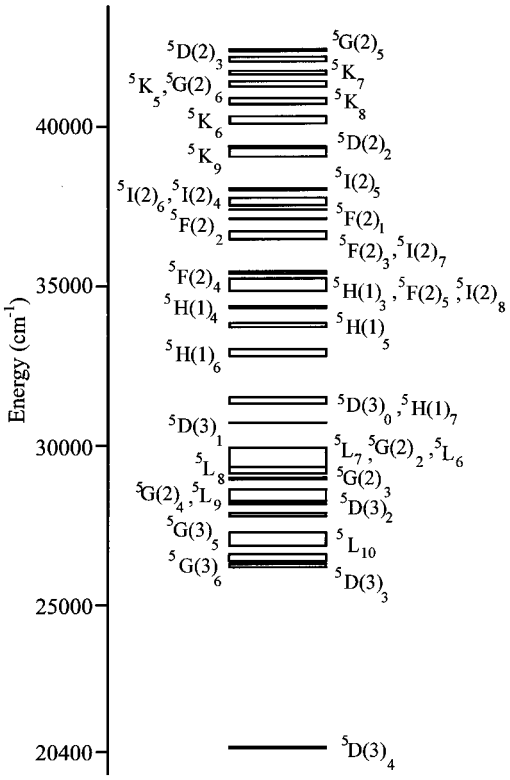

Figure 3. Energy diagram showing the locations and widths of all $4f^8[SL]J$ multiplet manifolds lying between 20 400 and 42 400 cm^{-1} for Tb^{3+} in TbODA. See Table 2 for greater detail.

In each of the systems represented in Table 4, the Tb^{3+} ions are located at 9-coordinate sites of trigonal symmetry, and in each system the coordination polyhedron formed by the nine ligand donor atoms about each Tb^{3+} ion has a slightly distorted tricapped trigonal prism structure. The Tb^{3+} donor atom coordination clusters in the respective systems are: $Tb^{3+}(Cl^-)_9$ in Tb^{3+}:$LaCl_3$; $Tb^{3+}(O^-)_6(N)_3$ in YbTbDPA ≡ $Na_3[Yb_{0.95}Tb_{0.05}(dpa)_3]\cdot NaClO_4\cdot 10H_2O$; and $Tb^{3+}(O^-)_6(O)_3$ in TbODA. In both TbODA and YbTbDPA, the negatively charged oxygen donor atoms are from ligand carboxylate groups and they are located at the vertexes of the trigonal prismatic coordination polyhedron. However, whereas the equatorial (prism-capping) coordination sites in YbTbDPA are occupied by pyridyl nitrogen atoms, these sites are occupied by ether oxygen atoms in TbODA.

The results shown in Table 4 reveal striking differences between the $Tb^{3+}(4f^8)$/crystal-field interactions in TbODA versus YbTbDPA. These differences are apparent in both the B_m^k parameter sets and the interaction strength quantities (S_{cf}^k and S_{cf}) determined for the respective systems. Except for the interactions represented in B_0^2 and B_6^6, the crystal-field interactions in TbODA are considerably stronger than those in YbTbDPA, and the S_{cf} strength quantity determined for TbODA is nearly 50% greater than that determined for YbTbDPA. This implies that the $-CH_2OCH_2-$ moieties of the $Tb(oda)_3^{3-}$ complexes in TbODA exert a much stronger influence on the $4f^8$ electronic energy-level structure of Tb^{3+} than do the pyridyl moieties of the $Tb(dpa)_3^{3-}$ complexes in YbTbDPA.

(36) Leavitt, R. P. *J. Chem. Phys.* **1982**, *77*, 1661.
(37) Chang, N. C.; Gruber, J. B.; Leavitt, R. P.; Morrison, C. A. *J. Chem. Phys.* **1982**, *76*, 3877.

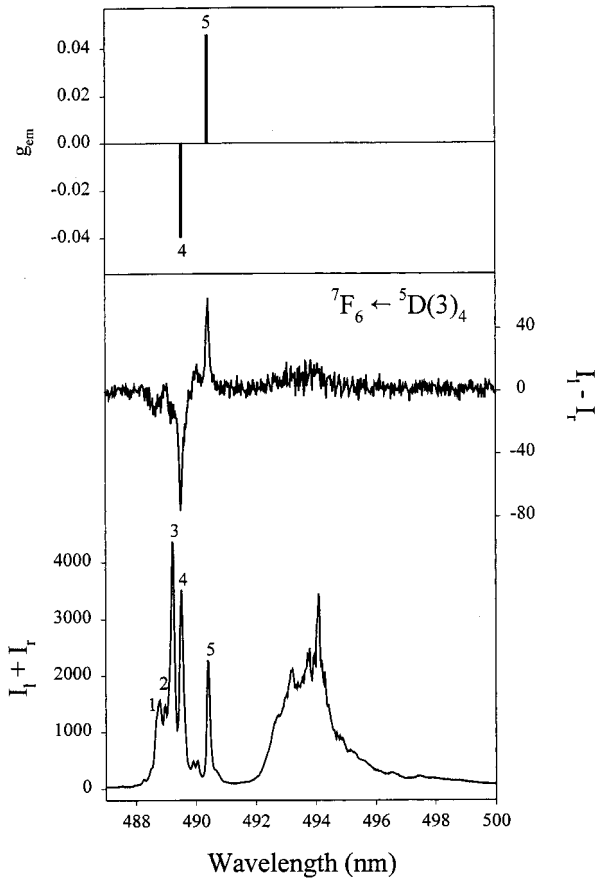

Figure 4. Spectra obtained from circularly polarized, axial emission measurements in the $^7F_6 \leftarrow {}^5D(3)_4$ transition region of $Tb^{3+}(4f^8)$ in TbODA. Sample temperature was ca. 20 K, and sample excitation was with the 351−364 nm output of an argon ion laser.

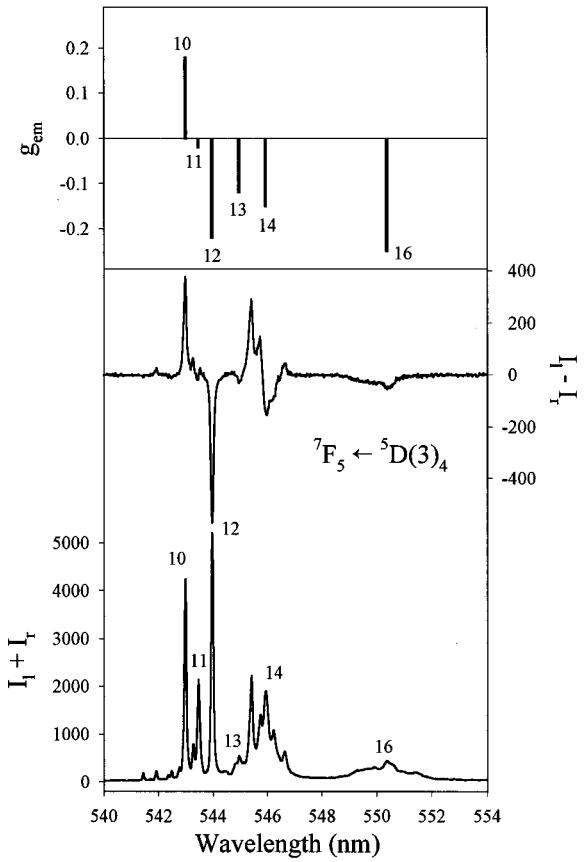

Figure 5. Spectra obtained from circularly polarized, axial emission measurements in the $^7F_5 \leftarrow {}^5D(3)_4$ transition region of $Tb^{3+}(4f^8)$ in TbODA. Sample temperature was ca. 20 K, and sample excitation was with the 488 nm output of an argon ion laser. See text for an explanation of peak numbering.

The comparative results shown in Table 5 for LnODA systems exhibit some expected and also some unexpected behavior across the lanthanide series. This is perhaps best demonstrated in the crystal-field interaction strength quantities (S_{cf}) determined for the eight systems. A trans-series plot of S_{cf} values is shown in Figure 1. The uncertainty bars in that plot reflect the uncertainties of the B_m^k parameter values used in calculating the relevant S_{cf}^k and S_{cf} quantities. We note first that if GdODA and TbODA are excluded from consideration, then the S_{cf} values exhibit a reasonably smooth *downward* trend across the series, and this is easily rationalized in terms of the relative radial extent (or spatial diffuseness) of the 4f electron orbitals in the earlier versus later members of the Ln^{3+}series. As one progresses across the series (from Nd^{3+} to Er^{3+}), the 4f electron charge distributions become more contracted (less diffuse) and, therefore, one expects their interactions with surrounding ligands or crystalline fields to become weaker. Since S_{cf} is defined as a measure of crystal-field interaction strength, one would expect a trans-series plot of S_{cf} values (for Ln^{3+} ions in any given host material) to show a smooth downward trend. The plot shown in Figure 1 conforms with this expectation only if the data points for GdODA and TbODA are excluded from consideration. It is not clear why GdODA and TbODA should show this apparently anomalous behavior in a trans-series comparison of crystal-field interaction strengths. However, it is well-known that in trans-Ln^{3+}-series comparisons of other physical properties (and some chemical properties), anomalous behavior is often observed for Ln^{3+} systems at or near the middle of the series (most often Gd^{3+}, but in some cases Eu^{3+} and Tb^{3+} systems). This is sometimes referred to as the "gadolinium break" in trans-series comparisons of lanthanide properties, and in a very general sense the results shown in Figure 1 could be placed under this rubric.

Spectra. In Figure 2 we show an energy diagram of all the *J* multiplet manifolds accessed in our optical emission experiments, and in Figure 3 we show an energy diagram of all the excited *J* multiplet manifolds located within the spectral range of our optical absorption measurements (20 400−42 550 cm^{-1}). In these figures, the widths shown for the various multiplet manifolds correspond to differences in energy between the highest and lowest crystal-field levels split out of the relevant $4f^8$[SL]*J* atomic-parentage states, and the locations of the multiplet manifolds are given relative to the lowest-energy crystal-field level of the $^7F_6$ (*ground*) multiplet manifold.

The total number of excited *J* multiplet manifolds accessible to our absorption spectra measurements was 39, all of which derive principally from Russell−Saunders terms with 5-fold (quintet) spin multiplicity. These multiplet manifolds span the 20 400−42 400 cm^{-1} energy range (above ground), and they contain a total of 281 crystal-field levels, 140 of which are doubly degenerate (E symmetry in the D_3 point group). Fifty of the E levels were located and assigned from our polarized absorption spectra measurements, and none of these levels showed any evidence of splitting under low-temperature sample conditions (down to ca. 10 K).

Most of the $^7F_6 \rightarrow$ excited *J* multiplet transition regions of $Tb^{3+}(4f^8)$ in TbODA exhibit highly congested absorption spectra that are very difficult to deconvolute into lines assignable to individual Stark-level-to-Stark-level transitions of well-defined

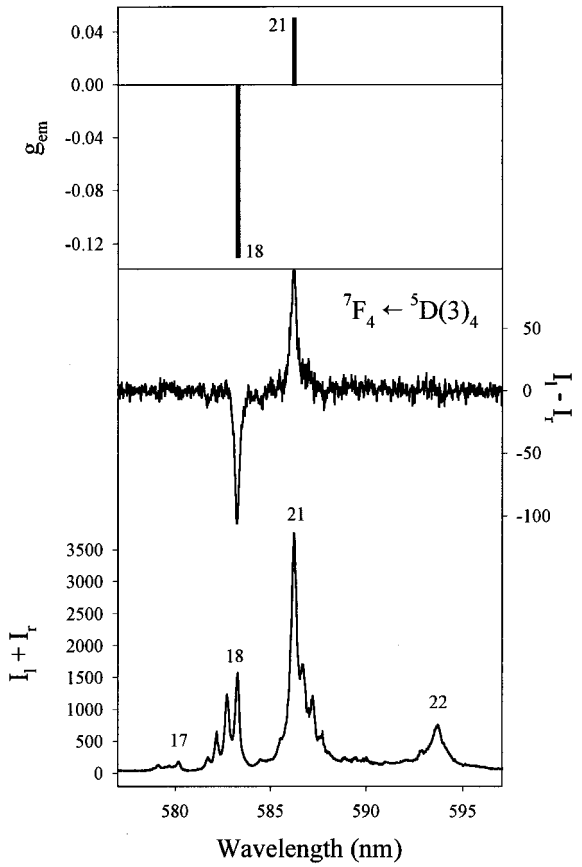

Figure 6. Spectra obtained from circularly polarized, axial emission measurements in the $^7F_4 \leftarrow {}^5D(3)_4$ transition region of $Tb^{3+}(4f^8)$ in TbODA. Sample temperature was ca. 20 K, and sample excitation was with the 488 nm output of an argon ion laser. See text for an explanation of peak numbering.

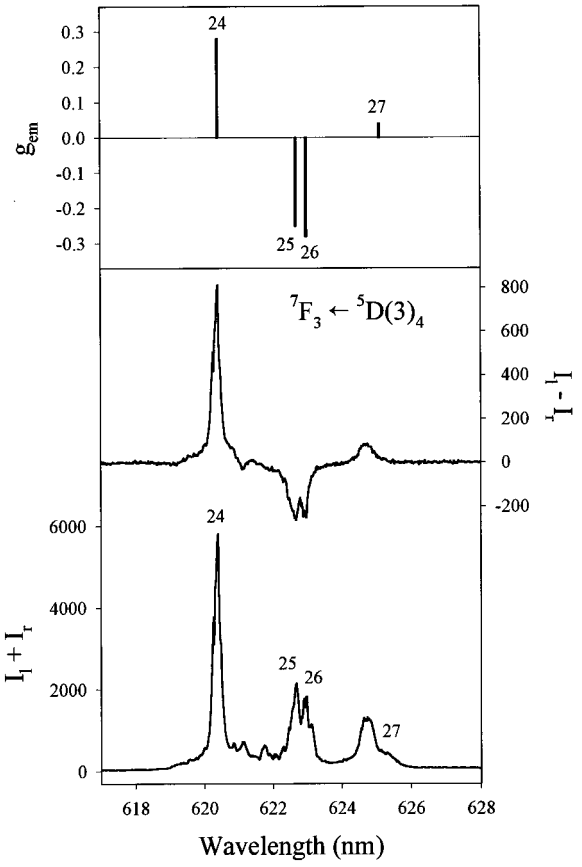

Figure 7. Spectra obtained from circularly polarized, axial emission measurements in the $^7F_3 \leftarrow {}^5D(3)_4$ transition region of $Tb^{3+}(4f^8)$ in TbODA. Sample temperature was ca. 20 K, and sample excitation was with the 488 nm output of an argon ion laser. See text for an explanation of peak numbering.

identities. This is due in large part to the relatively small spacings between the lowest-energy Stark levels of $^7F_6$ and to the high density of Stark levels in many of the excited *J* multiplet manifolds. Even spectra obtained at spectral resolutions <0.1 nm, on samples at low temperature, proved difficult to fully assign, in terms of individual Stark-level-to-Stark-level transition components. This accounts in large part for the relatively small number of energy levels (67 total) we list in Table 2 as being fully characterized within the 39 excited *J* multiplet manifolds probed in our optical absorption experiments. As was noted earlier, many more levels were located from our absorption (and CD) spectra measurements, but these additional levels could not be unambiguously assigned with respect to symmetry type.

In our previously reported studies of NdODA,[8,9] SmODA,[12−14] EuODA,[16,17] DyODA,[24] and HoODA[25−27] systems, we were able to obtain quantitative absorption line-strength data of sufficient quality and quantity to support detailed theoretical analyses. This was not possible for TbODA because too few lines in the absorption and CD spectra are sufficiently well resolved and characterized to permit quantitative line-strength determination and theoretical analysis. However, some parametric modeling calculations and simulations of polarized line intensity spectra were performed in the present study, using intensity parameters adapted from those derived previously for EuODA,[17] and the results obtained from these modeling exercises proved to be of some value in making line assignments in several difficult-to-interpret transition regions of the absorption spectra.

Optical emission spectra measurements were performed throughout each of the ^7F_J ($J = 0-6$) $\leftarrow {}^5D(3)_4$ transition regions of $Tb^{3+}(4f^8)$ in TbODA, and the results obtained from these measurements were used to locate and assign most of the crystal-field levels split out of the ^7F_J multiplets. These results were also used, in combination with our absorption measurement data, to characterize the crystal-field energy-level structure of $^5D(3)_4$. Both circularly polarized (*axial*) and linearly, σ and π polarized (*orthoaxial*) emission measurements proved to be crucial for making line assignments in the emission spectra. Here we will show only a few examples of the spectra obtained, focusing entirely on those in which chiroptical properties are displayed.

Figures 4−9 show spectra obtained from our measurements of left (l) and right (r) circularly polarized emission intensities (I_l and I_r) throughout the ^7F_J ($J = 0-6$) $\leftarrow {}^5D(3)_4$ transition regions of $Tb^{3+}(4f^8)$ in TbODA, at a sample temperature of ca. 20 K. The bottom spectrum in each figure is a plot of ($I_l + I_r$) versus emission wavelength, the middle spectrum is a plot of ($I_l - I_r$) versus emission wavelength, and the top, bar spectrum show emission dissymmetry factors, $g_{em} = 2(I_l - I_r)/(I_l + I_r)$, measured at several wavelengths in the emission spectra. The spectral features (and bars) labeled with numbers identify the locations of transitions that originate from the lowest E level of $^5D(3)_4$ (i.e., level 34 in Table 2) and terminate on one of the Stark levels of the relevant ^7F_J multiplet manifold. The numeric labels on the features identify the terminal levels (according to the level numbers specified in Table 2). None of the spectral features assigned to transitions from higher-lying crystal-field levels of $^5D(3)_4$ (e.g., level nos. 36−39) are labeled in Figures 4−9. In each figure, the sum ($I_l + I_r$) and difference ($I_l - I_r$) emission intensity scales are expressed in identical, but otherwise arbitrarily chosen, intensity units.

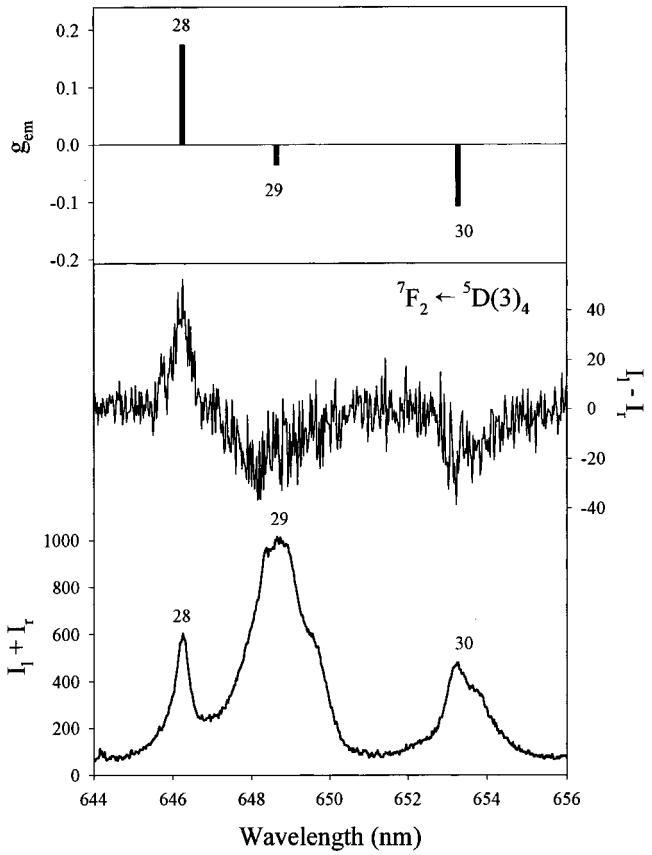

Figure 8. Spectra obtained from circularly polarized, axial emission measurements in the $^7F_2 \leftarrow {}^5D(3)_4$ transition region of $Tb^{3+}(4f^8)$ in TbODA. Sample temperature was ca. 20 K, and sample excitation was with the 488 nm output of an argon ion laser. See text for an explanation of peak numbering.

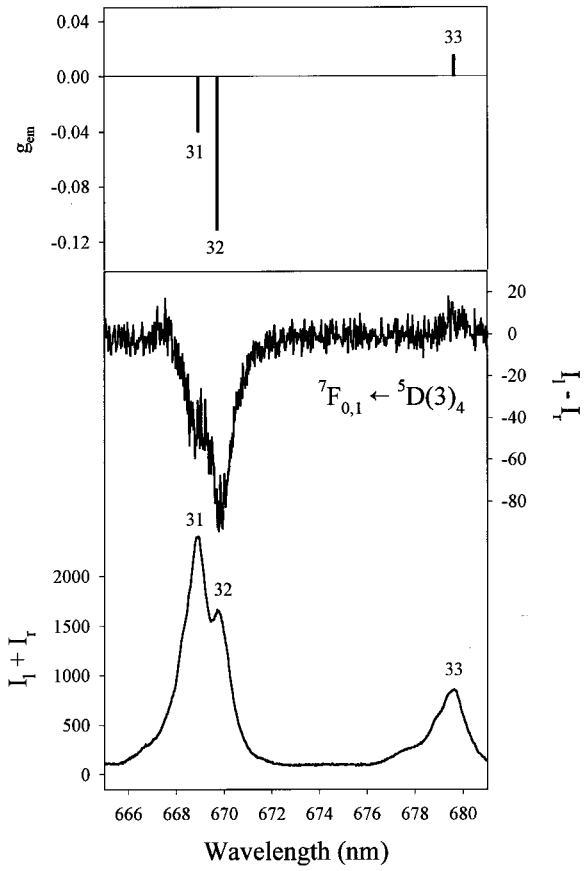

Figure 9. Spectra obtained from circularly polarized, axial emission measurements in the $^7F_{0,1} \leftarrow {}^5D(3)_4$ transition regions of $Tb^{3+}(4f^8)$ in TbODA. Sample temperature was ca. 20 K, and sample excitation was with the 488 nm output of an argon ion laser. See text for an explanation of peak numbering.

The $(I_l - I_r)$ spectra shown in Figures 4−9 are commonly referred to as *circularly polarized luminescence* (or CPL) spectra,[2,39] and they carry information about the *chirality-dependent* properties of optical emission processes in TbODA. These spectra are the emission analogues of circular dichroic absorption spectra (or CD spectra), which carry information about the chirality-dependent properties of optical absorption processes. The circular differential emission intensity quantities, $\Delta I = I_l - I_r$, and emission dissymmetry factors, $g_{em} = 2\Delta I/(I_l + I_r)$, measured in CPL spectroscopy are analogous to the circular differential absorptivity quantities, $\Delta\epsilon = \epsilon_l - \epsilon_r$, and absorption dissymmetry factors, $g_{ab} = 2\Delta\epsilon/(\epsilon_l + \epsilon_r)$, measured in CD spectroscopy. It has become common practice in both CD and CPL spectroscopy studies to use the dimensionless absorption and emission dissymmetry factors, g_{ab} and g_{em}, as measures of the *degree* and *sense* of chiroptical activity in individual absorption and emission lines (and their corresponding transitions). The magnitudes and signs of these quantities depend on the mechanistic details of the transitions under study, and they also depend on the degree and sense of structural chirality in the optically active absorbing or emitting species.

For most electronic transitions observed in the great majority of optically active (chiral) systems, the largest contributions to CD or CPL line strengths derive from interferences between electric and magnetic dipole transition amplitudes in the underlying optical processes.[2,39] The dissymmetry factors observed in the CD/absorption and CPL/emission spectra of these transitions may be expressed as

$$g_{ab}(i) = \frac{4|\mathbf{P}_i||\mathbf{M}_i|\cos\theta_i}{|\mathbf{P}_i|^2 + |\mathbf{M}_i|^2} \tag{7}$$

$$g_{em}(j) = \frac{4|\mathbf{P}_j||\mathbf{M}_j|\cos\theta_j}{|\mathbf{P}_j|^2 + |\mathbf{M}_j|^2} \tag{8}$$

where i and j are transition labels; $\mathbf{P}_{i(j)}$ and $\mathbf{M}_{i(j)}$ denote, respectively, the electric and magnetic dipole transition vectors of the indicated absorptive (or emissive) transition; and $\theta_{i(j)}$ is the angle between $\mathbf{P}_{i(j)}$ and $\mathbf{M}_{i(j)}$. In our discussion here, it will be useful to reformulate eqs 7 and 8 to show the dependence of $g_{ab}(i)$ and $g_{em}(j)$ on the *ratios* of electric and magnetic dipole transition amplitudes:[40]

$$g_{ab}(i) = \frac{4(P_i/M_i)\cos\theta_i}{(P_i/M_i)^2 + 1} \tag{9}$$

$$g_{em}(j) = \frac{4(P_j/M_j)\cos\theta_j}{(P_j/M_j)^2 + 1} \tag{10}$$

where $P_{i(j)}$ and $M_{i(j)}$ represent the magnitudes (or lengths) of the transition vectors $\mathbf{P}_{i(j)}$ and $\mathbf{M}_{i(j)}$. These expressions show

(38) Jayasankar, C. K.; Reid, M. F.; Richardson, F. S. *J. Less-Common Met.* **1989**, *148*, 289.
(39) Riehl, J. P.; Richardson, F. S. *Chem. Rev.* **1986**, *86*, 1.
(40) Metcalf, D. H.; Richardson, F. S. *J. Alloys Compd.* **1994**, *207/208*, 59.

that the values of $g_{ab}(i)$ and $g_{em}(j)$ will approach their upper and lower limits (+2 and −2) when $\cos \theta_{i(j)} = \pm 1$ and $(P_{i(j)}/M_{i(j)}) \rightarrow 1$.

In axially symmetric optically active chromophores or luminophores, such as $Tb(oda)_3^{3-}$ complexes in TbODA, the $\mathbf{P}_{i(j)}$ and $\mathbf{M}_{i(j)}$ vectors of each dipole-allowed transition must be either parallel or antiparallel (i.e., $\theta_{i(j)} = 0$ or 180°), and, therefore, the $\cos \theta_{i(j)}$ functions for all of the CD and CPL active transitions are constrained to values of ±1. It follows that the magnitudes of the dissymmetry factors observed for these transitions are determined entirely by the $P_{i(j)}/M_{i(j)}$ ratios shown in eqs 9 and 10. Most of the transitions observed in the CD/absorption and CPL/emission spectra of TbODA exhibit $|g_{ab}|$ or $|g_{em}|$ values that are <0.3, which implies that the $P_{i(j)}/M_{i(j)}$ ratios for most of these transitions are either >13 or <0.08. The largest dissymmetry factors are observed in the $^7F_{3,5} \leftarrow {}^5D(3)_4$ transition regions of the CPL/emission spectra (see Figures 5 and 7). Results obtained from our linearly (σ versus π) polarized emission measurements show that many of the lines observed in these transition regions exhibit significant admixtures of electric *and* magnetic dipole character.

Conclusion

Among all the LnODA systems examined to date, TbODA posed the most difficult challenges for crystal-field energy-level location, assignment, and analysis. The $4f^8(Tb^{3+})$ electronic state structure in TbODA is relatively dense, and there is extensive mixing and overlapping between and among many of the excited *J* multiplet manifolds. Location and assignment of crystal-field levels required use of the full complement of spectroscopic measurements performed in this study: unpolarized, linearly polarized, and circularly polarized optical absorption and emission measurements on single-crystal samples over a wide range of sample temperatures. The energy-level modeling calculations performed in this study produced reasonably good fits between calculated and experimentally observed energy-level structure in the $4f^8$[SL]*J* multiplet manifolds of Tb^{3+}, and they proved sufficient for characterizing the 4f electron/crystal-field interaction strengths and anisotropies in TbODA. The overall crystal-field interaction strength (S_{cf}) determined for TbODA was found to be ca. 45% greater than that determined for DyODA, and it is greater than those determined for all other members of the LnODA series. The degree of chiroptical activity observed in the CD/absorption and CPL/emission spectra of TbODA is somewhat greater than that observed for most optically active systems, but it is comparable to that observed in the analogous spectra of other LnODA systems. The relatively strong chiroptical activity exhibited by TbODA and the other LnODA systems reflects, in large part, the relatively strong admixtures of electric *and* magnetic dipole strength in the 4f−4f transitions of these systems.

Acknowledgment. This work was supported by the U.S. National Science Foundation.

IC971114N